Estuaries and Coasts (2022) 45:1270–1286
https://doi.org/10.1007/s12237-021-01025-x

Modeling Salinity Response to Relative Sea Level Rise in a Brackish Floodplain Region

Robert L. Miller[1]

Received: 31 May 2021 / Revised: 15 October 2021 / Accepted: 4 November 2021 / Published online: 15 November 2021

Abstract
A model-based assessment of the response of mean salinities to relative sea level rise (RSLR) in a brackish floodplain region is presented. The study area is located on the Gulf coastal region of Louisiana which is experiencing some of the highest rates of relative sea level rise in the world. A two-dimensional modeling approach is developed, and the local hydrodynamic model is well calibrated for scenario testing purposes. Numerous alternative scenarios of RSLR are evaluated to simulate the salinity response in both the open water and adjacent floodplain areas under a range of wetland roughness and dispersion factors. The analysis reveals key insights on the mean salinity response patterns to RSLR including the sensitivity to deterioration of wetlands and offshore boundary conditions. Also developed are expressions describing the qualitative nonlinear response. A novel partitioning strategy is also employed in the simulation trials to analyze the effect of various accretion deficit scenarios on the nonlinear RSLR-induced salinity response. The analysis shows that the fraction of the floodplain which is able to keep pace with RSLR has an effect an order of magnitude larger than transport parameters associated with marsh deterioration on the RSLR salinity response. Sites exhibiting sustained accretion surpluses over the long term are able to keep pace and would likely contribute to greater overall resilience to future RSLR-induced salinity changes. The robust scenario analysis and findings of this study are widely applicable to the global challenge of managing the effects of RSLR in coastal wetland areas.

Keywords Relative Sea Level Rise · Salinity Response · Brackish Region · Accretion Deficit · Numerical Modeling

Introduction

Relative sea level rise is a critical challenge facing coastal regions worldwide (Church and White 2011). Ambient sea levels play a role in coastal flood risk management and are a significant driver of coastal wetland ecosystem dynamics (Morris et al. 2002). Sea level rise and inland salinity encroachment have been identified as key processes which can accelerate coastal land loss (Reed et al. 2020). Salinity levels and various forms of hydrologic stress (e.g., prolonged inundation) affect wetland population dynamics. These interacting factors affect growth, reproduction, mortality, and ultimately wetland species persistence (Spalding and Hester 2007; Pathikonda et al. 2008). Moreover, salinity affects estuarine fish population dynamics and inland salinity encroachment threatens the future availability of freshwater supplies used for irrigation and drinking (Sunde et al. 2018; Krvavica et al. 2012). As such, the relationship between future sea level rise and salinity is a critical factor in coastal protection, ecological, and water resource management resiliency (Rice et al. 2012).

Numerous studies have addressed the link between relative sea level rise and future salinities (Hong and Shen 2012; Vargas et al. 2017; Bhuiyan and Dutta 2012). Process-based mathematical models have been successfully used for these purposes. A three-dimensional (3-D) hydrodynamic model was used to assess the relative sea level rise (RSLR)–induced salinity response in the Wu River estuary in Taiwan (Liu and Liu 2014). 3-D modeling was also used to study this response under high and low flow regimes with an emphasis on the growth rates of oysters in Apalachicola Bay (Huang et al. 2015). Yang et al. (2015) similarly used a 3D modeling approach (FVCOM) to study changes involving RSLR-induced salinity response coupled with land use and river inflows in the Snohomish River estuary. Recently, a two-layer approach was employed to study saltwater wedge

Communicated by Neil Kamal Ganju

✉ Robert L. Miller
robert.miller@louisiana.edu

[1] Department of Civil Engineering, University of Louisiana at Lafayette, P.O. Box 43598, Lafayette, LA 70504-3598, USA

dynamics in the Neretva River estuary (Krvavica and Ruzic 2020). Shallow estuaries are often well approximated with 2D analysis depth-averaged approaches as was recently demonstrated by Vargas et al. (2017) in their study on the RSLR-induced salinity response in the Ria de Aveiro estuary. Thus, physics-based models (having varying spatial resolutions based on the study objectives and key system attributes) can serve as valuable management tools to quantify the problem of RSLR-induced salinization.

The existing modeling literature generally focuses on the RSLR-induced salinity responses in the open water components of the estuary (i.e., tidal bays and rivers). Additional study is needed to investigate the RSLR-induced salinity effects in the floodplain areas adjacent to the open water bodies in estuaries. This point is salient for inquiry centered on land loss and sustainability of wetland plant ecosystems. Such investigations would naturally extend upon the rich body of existing research focusing on the primary open water hydraulic components. However, the response of coastal floodplains to RSLR-induced salinity is not straightforward as it will likely depend on biological components (e.g., wetland vegetation dynamics) which evolve in response to changes in flooding and salinity regimes (Reed and Cahoon 1993; Morris et al. 2002). Changes in landscape elevations would also likely play a major role in the overall response (Reed and Cahoon 1993; Fagherazzi et al. 2019; Morris et al. 2002). Process-based approaches aimed at gaining quantitative insights on the RSLR-induced salinity response in coastal floodplains should begin to account for these dynamic factors — a task undertaken in this paper.

The objective is to present a process-based study aimed at understanding the sea-level rise salinity response in a brackish-water coastal floodplain located in the Vermilion Bay estuary in south-central Louisiana, USA. Coastal Louisiana is experiencing some of the world's highest rates of relative sea-level rise, and large-scale interventions are being undertaken to mitigate these effects (Jankowski et al. 2017; White et al. 2019a, b; Cahoon 2015). One of the challenges of using physically based modeling to address the sea level induced salinity response is the dynamic coastal floodplain which responds to persistent changes (e.g., RSLR) by deterioration (i.e., vegetation dieback) or by dynamically adjusting its elevation to establish a new equilibrium. These anticipated adjustments should be factored into a modeling-based framework. To meet these study objectives, a description of the setup and calibration of a two-dimensional model for hydrodynamics and depth-integrated salinities and the development of numerous simulation trials aimed at gaining quantitative insights into the relative sea-level rise/salinity response patterns within the floodplains are described. In addition to sea level forcing, the scenario trials analyze a range of physical parameter combinations (Manning's n and horizontal dispersion coefficients) which are generally well correlated with wetland vegetation characteristics affecting saltwater transport within floodplain habitats. An examination is also made on the role of the accretion deficit in shaping the RSLR-induced salinity response by quantitatively investigating the role played by dynamic elevation adjustments.

This paper is organized in the following manner. In "Methods," the setup is described along with the field data collection and calibration efforts, as well as the methodology for the simulation trials. In "Results," the scenario results and analysis are presented and in "Discussion" is a summary of the findings from the study, modeling uncertainties, and offer topics for future research. "Conclusions" presents the main conclusions of this study.

Methods

A two-dimensional hydrodynamic and salinity modeling approach is employed to analyze various alternative scenarios which simulate the sea-level rise salinity response in the Avery Island, LA coastal wetlands. Notably, analysis of gauge records suggests that Louisiana is subject to some of the most rapid sea level rise rates in the world (Penland and Ramsey 1990).

Description of the Study Area

The Avery Island study area is located in the subtropical Teche/Vermilion basin of coastal Louisiana (Fig. 1). This region receives discharge from rainfall-runoff emanating from watershed areas located upstream (tributary points labeled $Q1, \ldots, Q5$) as well as tidal influence via Vermilion Bay located to the south. The overall watershed area encompasses 519 km^2 of total drainage area. The upland portions of this watershed study region are primarily dominated by agricultural land use (60–65%) based on GIS analysis of land cover data. Field visits further suggest that the remaining land uses include aquaculture and rice production and relatively small urban areas clustered around municipal centers as well as wetlands which dominate the areas southward of the coastal zone boundary (CZB). The wetland plant types vary from cypress-tupelo swamps (observed in field visits) along the northerly fringe of the coastal zone while transitioning to the dominant marsh species (e.g., *Schoenoplectus americanus* and *Spartina patens* based on floristic quality indices at Coastwide Reference Monitoring System (CRMS) stations 511 and 531 moving southerly towards Vermilion Bay. Soils are generally poorly drained (e.g., Jeanerette silt loam and silty clay loam) based on evaluation of soil data (USDA 2021). Yearly precipitation at the nearby Acadiana Regional Airport Cooperative Station National Climatic Data Center site averages 152 cm. Fontenot (2004) suggests

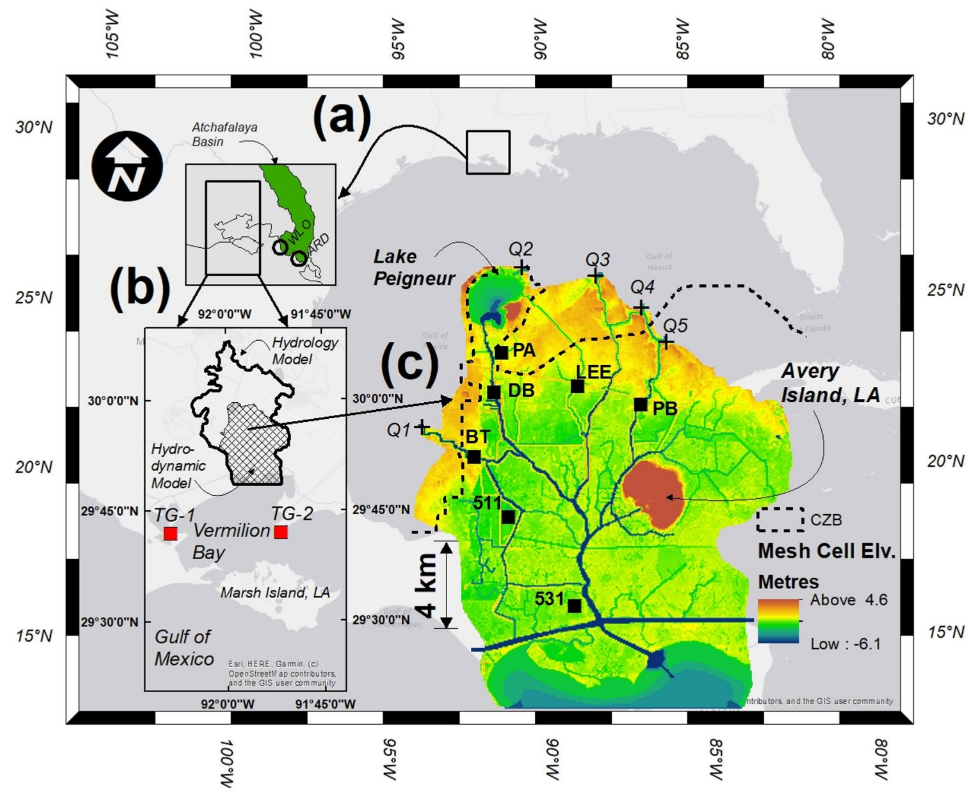

Fig. 1 (**a**) Overall study area relative to the Atchafalaya Basin. The circles represent the Wax Lake Outlet (WLO) and Atchafalaya River Delta (ARD) freshwater outflow points whose plume influences salinities in the area. (**b**) Vermilion Bay closer view of the study area showing the regional hydrology model limits and local hydrodynamic model domain(s). TG-1 (USGS 07387050) and TG-2 (USGS 07387040) are tide gauges used to provide downstream boundary conditions for the local model. (**c**) Local hydrodynamic model mesh, Louisiana coastal zone boundary (CZB) limits and key geographic features. The crosses indicate tributary inflow points provided by the regional hydrology model while black squares represent gauges used in the calibration effort

that yearly reference evapotranspiration generally ranges between 120 and 140 cm in Louisiana.

Salinities below the coastal zone are influenced not only by local hydrology but also by runoff occurring at the Atchafalaya River (ARD) and Wax Lake Outlet (WLO) deltas located to the east (Mossa 2016). Review of the Cypremort Point tide gauge salinities in Vermilion Bay suggests that the outflow plume generally meanders westward with the alongshore current and greatly affects salinities in the bay. Evaluation of discrete field data collected by the author since 2014 suggests that salinities in the study area typically range from 0 to 2 psu from winter through the early summer periods with an increase occurring in mid-summer as a result of the receding WLO/ARD freshwater plume. Higher salinities prevail during the fall with values often ranging from 2 to 5 psu particularly when discharge is at a minimum on the Atchafalaya River with locally higher spikes during droughts and storm surge events. The tide gauge data suggests that tidal amplitudes are on the order of 50 cm during a common tide cycle, although local weather patterns (e.g., frontal systems, tropical storms) play a significant role in local tidal water level variations.

The floodplains consist of emergent vegetation including cypress-tupelo swamp along the limnetic upland fringe with the typical transition to common marsh plant species moving along a seaward trajectory (Visser et al. 2000). A review of the available CRMS (stations 511 and 531) vegetation data suggests the existence of a gradient of marsh types ranging from oligohaline (0.5–5) near the CZB to mesohaline types (5–18) occurring along the downstream fringe near Vermilion Bay.

An extensive network of open channels exists across the floodplain regions. GIS measurements show the top widths of the primary channels generally range from 15 to 120 m, and field measurements suggest channel depths of 1.5 to 4 m. The channel network has been extensively altered over the years to facilitate more rapid drainage of runoff from adjacent agricultural and municipal lands. The most typical types of hydro-modifications of the main flow paths are straightening and dredging of natural channels as well as the placement of spoil banks along dredged reaches. The spoil banks feature prominently in the region and heights of 2 m above adjacent grade are common (based on GIS review of elevation data). In addition to local drainage, the channel network has also been altered for navigation. The navigation interests are mostly related to the heavy oil and gas production and mining industries and offshore exploration and commercial fishing activities which are present in the area. Of considerable local interest and geomorphological relevance are the prominent geo-topographic features associated with the salt-dome islands (e.g., Jefferson and Avery Island) as well as Lake Peigneur located adjacent to Jefferson Island (Hernandez et al. 1976). Lake Peigneur was historically 2–3 m deep prior to an infamous salt mine collapse of 1980 which abruptly deepened and expanded the southeastern corner of the lake considerably (Autin 2002).

Modeling Approach

Two MIKE 21 numerical models were deployed for the analysis — a regional watershed model to capture the rainfall-runoff hydrology and a local model having a higher spatial resolution for the area of interest. MIKE 21 has been widely used to study salinity circulation in the adjacent Chenier Plain of coastal Louisiana (Miller and Meselhe 2007). The sole purpose of the regional model was to generate rainfall runoff hydrographs from the contributing watershed areas upstream of the main study area, and salinity was not simulated with this model. Rainfall-runoff was generated using a rain-on-grid (RoG) approach. This method allows for the specification of hourly inflow boundaries to the local model in the absence of discharge measurements in this area. The use of MIKE 21 to simulate the overland hydrology also avoids some of the difficulty associated with deploying more traditional hydrologic models (e.g., HEC-HMS) in extremely flat coastal regions. In these areas, key parameters such as time of concentration and unit hydrograph peaking factors may not be well defined. The regional model was extended upland all the way to the watershed boundary so as to capture all rainfall-runoff inflows. Hence, no additional boundary inputs were required in this model.

The local MIKE 21 model also conformed to the regional watershed boundaries but was confined to the lower portions surrounding the coastal zone where a higher resolution is appropriate. Given the nested spatial configuration of the two models, future adjustments of the coastal zone boundary can be reflected by moving the upland extents of the local model further inland. The runoff hydrographs at the handoff points can thusly be easily adjusted for the new configuration. This approach provides flexibility in implementing future boundary conditions at the upland/coastal interface which can be difficult in ungauged low-gradient systems such as this one (Saad et al. 2020). The local model analyzes both hydrodynamics and salinity transport which are the main focus of this study. The shallow water model approximation, advection–dispersion transport model, and numerical integration procedures employed in MIKE 21 have been described by others elsewhere (e.g., see (DHI 2017)).

Model Setup

The study area projected coordinate system was taken as Universal Transverse Mercator (UTM) zone 15. The regional hydrology model occupies an area of 519.4 km^2 and consists of square grid cells having a resolution of $\Delta x = \Delta y = 100$ m for a total of 51,943 computational points. The local hydrodynamic model consists of 62,467 computational points having a structured mesh resolution of $\Delta x = \Delta y = 63$ m. The local model north–south extents were selected to encompass the current CZB while extending into Vermilion Bay far enough to provide a suitable boundary condition. The east–west extents were based on a watershed delineation using GIS analysis based on 5 m $\times$ 5 m light detection and ranging (LiDAR) digital elevation model contours (Cunningham et al. 2004). Mean land elevations in the local hydrodynamic model are 0.54 $\pm$ 1.44 m NAVD 88 G99.

Above-water ground elevations were resampled from available LiDAR DEM. Underwater bathymetry elevations were inferred based on a review of available navigation charts (NOAA 2021) and depth measurements taken at various access points by the author. These datapoints coupled with prior studies on similar channels in the surrounding regions were used to inform the manual creation of underwater bathymetric contours. For channels narrower than the grid spacing, the bottom elevations were selected with the goal of preserving the mean cross-sectional area. This seamless process also controlled for spurious discontinuities which may occur when implementing automated interpolation-based grid generation methods or from the resampling process itself. Marsh connectivity was also enforced in the resampled grid by inspection of available aerial photos, LiDAR, and deployment of a DEM conditioning (i.e., "burning") procedure based on manually delineated connection pathways. Spoil banks and road embankments were also captured in the manual grid creation process to ensure that the resampled grid more accurately reflects key aspects affecting the circulation of water and salinity within the system.

Since there were no discharge gauges located in the area at the time of the study, the regional model was used to furnish instantaneous estimates of rainfall runoff hydrographs entering the primary area of interest (local hydrodynamic model) at tributary points. Hydrologic losses were lumped together as the sum of losses due to evapotranspiration of surface waters and infiltration losses into the soil. A simple uniform and constant loss rate of 5 mm/day was calculated from nearby meteorological measurements applied to the Penman–Monteith equation and was applied to both regional and local models. This value was also the result of an assumption that evapotranspiration was the predominant loss mechanism given the poorly drained soil types and relatively frequent precipitation events occurring in this subtropical area during the summer study period. Flow rates were extracted from the regional model at key tributary points (Fig. 1) and used as discharge boundary inputs into the local hydrodynamic model. Inflow concentrations were assigned a background value of 0.05 psu based on review of salinity samples taken after several heavy rain events.

Precipitation inputs into both models were furnished by an hourly rain gauge located nearby to the study area (LSU AgCenter — Iberia Research Station). This gauge also provided wind speed and direction information for the models on an hourly timescale (Price 2020). Offshore boundary conditions and boundaries on the Gulf Intracoastal Waterway (GIWW) for water level (hourly) and salinity (daily) were provided by available measurements at nearby tide gauges. Given the influence of the Atchafalaya outlets on Vermilion Bay salinities, the salinity time series in Vermilion Bay was developed as a composite of the United States Geological Survey (USGS) salinity readings at the east and west tide gauge locations. The model simulation period of analysis was May 1, 2020 to October 18, 2020.

Field Data

At the time of this study, two stations featuring publicly accessible data were available in the study area at locations to serve as water level and salinity calibration points (CRMS 511, 531). Given the relatively large size of the study area, an additional field data collection campaign was undertaken by the author. Synoptic samples of conductivity, salinity, dissolved oxygen, water temperature, and relative water surface elevation as well as estimates for surface flow direction were obtained. An intensive measurement campaign was conducted during the study period from May 1, 2020 to October 18, 2020. Measurements at three locations (PB, LEE, and PA) were taken from bridge structures so as to obtain vertical variation in salinities within the water column when feasible (Fig. 2). This was done in order to verify the well-mixed assumption inherent in the vertically integrated MIKE 21 modeling approach being applied for this study. Note that additional measurements (not shown) were also taken on the tributaries beyond the coastal zone boundary to estimate the upstream limits of the local hydrodynamic model based on consistently fresh salinity readings.

The salinity, temperature, and dissolved oxygen measurements were taken using a handheld YSI-556 multiparameter water quality sonde, and in most cases, top and bottom salinities were measured along with vertical profiles when water velocities did not prevent accurate profiling from occurring. The relative water surface elevations were measured directly via top-of-water tape-down estimates which converted to water surface elevations where feasible based on manual review of geo-referenced raw LiDAR points and measurements taken at the sites. A total of 298 sampling visits were taken yielding 126 discrete stage measurements and 494 top and bottom salinity samples, including 49 full-depth salinity, temperature, and dissolved oxygen profiles (0.61-m increments at location "PB"). The discrete salinity and water surface elevation measurements were used to calibrate the local

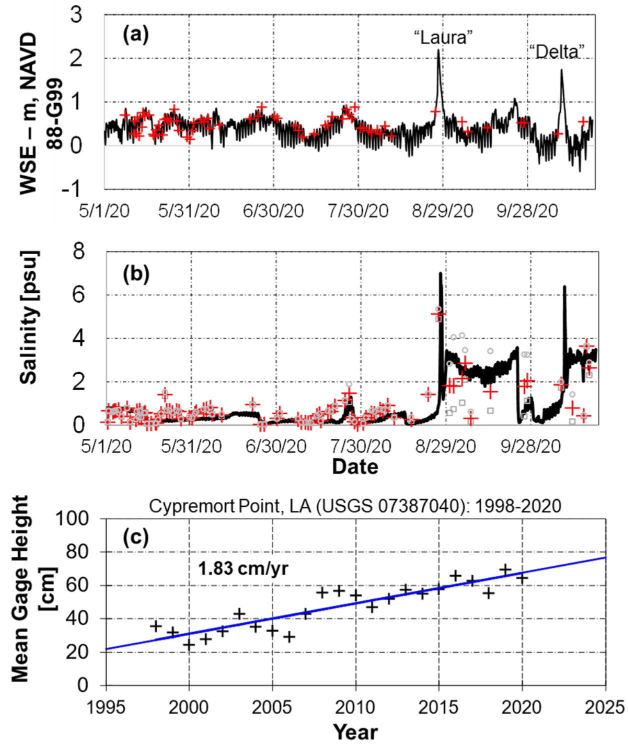

Fig. 2 (**a**, **b**) Field measurements (red crosses, grey squares and circles) vs. model outputs (black solid lines) at location "PB." (**a**) Stage simulation vs. stage measurements (red crosses). (**b**) Simulated depth-averaged salinities vs. top (gray squares), bottom (gray circles) and depth averaged measured salinities (red crosses). Names in quotes refer to hurricanes which affected the study area in 2020. (**c**) Recent trend in annual mean gauge heights for the nearby tide gauge TG-2 (see Fig. 1 for the gauge location)

hydrodynamic model supplemented by the continuous CRMS measurements (Coastal Protection and Restoration Authority (CPRA) of Louisiana 2021). Depth soundings at approximately mid-channel were inferred at each site where salinity profiles were collected during each visit as a result of the profiling routine. The soundings were checked via tape-down measurements taken during slack water periods.

The region was affected by storm surge from the passage of two hurricanes — Laura and Delta during the latter half of the study period. Salinities at the sample points were mostly well mixed, but location PB became moderately stratified for several weeks after the first hurricane (estuarine Richardson number 0.3–0.5). All salinity measurements were converted to depth-averaged estimates for the sake of consistency in calibrating the salinity model. Given the shallowness of the system and relatively low levels of salinity stratification observed at most field sample locations except immediately following a hurricane storm surge, the two-dimensional depth-averaged modeling approach was sufficient for the purposes of the study.

Model Parametrization

Beyond the upstream tributary inflows (from the regional hydrology model) and offshore boundary forcing conditions, the main processes analyzed in the local hydrodynamics model include bed resistance, wind stress, and turbulent eddy viscosity. For this study, the main model calibration parameter was taken as the bed roughness which is modeled in MIKE 21 via the Chezy friction term. Spatially varying Manning's numbers were specified. This approach allows for MIKE 21 to implement a depth-dependent (hence time-varying) spatially distributed bed resistance which is obtained via the relationship $C = Mh^{\frac{1}{6}}$. A spatially varying Manning's M map ($M = 1/n$ where n is the Manning's resistance value) was developed by a simple land–water classification scheme. The Freshwater Canal tide gauge (NOAA/NOS/CO-OPS 8,766,072) was used to establish a mean tide level (MTL) of + 0.15 m NAVD 88 G99, whereby all mesh elements having an elevation less than MTL were classified as water with the remaining cells classified as land. Land elements were assigned a roughness value of $n = 0.07$ ($M = 14.3$), and water elements were given a value of $n = 0.015$ ($M = 65$). The base Manning's n values of 0.07 and 0.015 approximately correspond to vegetated marsh/marsh platform and muddy sea bed conditions respectively (e.g., Table 2 in Sullivan et al. (2015)).

The wind stress term was presumed to be the next most significant process affecting the hydrodynamics in the area. Wind effects are significant in the computation of water stages in the area. The time-varying wind stress is implemented in MIKE 21 using the following sub-model for the wind friction factor:

$$f(V) = \begin{cases} f_0, & V \le V_0 \\ f_0 + \frac{V-V_0}{V_1-V_0}(f_1 - f_0), & V_0 \le V \le V_1 \\ f_1, & V > V_1 \end{cases} \quad (1)$$

Here, V is the time-varying wind speed (m/s) being applied, and $V_0 = 0.0$ m/s and $V_1 = 30$ m/s. The recommended values for the wind friction factor are $f_0 = 0.00063$ and $f_1 = 0.026$ (representative of open sea conditions). To simplify the computations, a constant wind friction factor of $f = 0.021$ was employed uniformly across the local hydrodynamic model domain. A constant flux-based eddy formulation was utilized with the eddy viscosity of $E = 3.0$ applied uniformly throughout the analysis noting that this parameter value improved model stability but did not play a major role in stage performance overall.

The horizontal dispersion coefficients were the main parameters used in calibrating the salinity transport model. Salinity circulation within the system is mainly governed by transport due to advection and dispersion which models additional transport due to the combined effects of unresolved flow processes. Such processes include shear due to gradients in spatial velocity fields as well as diffusion effects due to molecular motions and (more significantly) turbulence. A key difficulty in estimating the dispersion coefficients when dealing with spatial discretization is the characterization of these non-resolved scales which can depend significantly on local bathymetry configuration, density gradients, and wind. As such, the general assumption taken in this effort is that the dispersion coefficients should vary directly with the model resolution Δx over which larger values should correspond with a greater degree of sub-grid dispersive effects. As such, the following strategy was used to estimate the dispersion coefficients

$$D_x = \max(K\Delta xu, D_{x,\min}) = \max(Eu, D_{x,\min}) \quad (2)$$

where D_x is the dispersion coefficient (m^2/s), K is a dimensionless constant, and Δx is the grid spacing (m). $D_{x,\min}$ is the minimum dispersion coefficient and identical sub-models applied for the dispersion coefficient in the y-direction, D_y. For this study, $K = 0.24$ was taken for an effective proportionality constant E of 15.0 which is within the range of previous studies in coastal Louisiana (Miller and Meselhe 2007). A minimum dispersion coefficient was imposed to represent dispersive transport which occurs when depth-averaged velocities become very small — as would often be the case in shallow flow across vegetated floodplain wetland areas. The minimum value of $D_{x,\min} = D_{y,\min} = 0.05\mathrm{m}^2/\mathrm{s}$ was applied based on suggested typical values for wetland areas in a mesoscale tracer study conducted in the Florida Everglades (Ho et al. 2009).

Model Skill Assessment

The skill of the model was assessed based on simulated values compared against instantaneous measurements of water level and salinity. In addition to qualitative assessment of the model performance and the Pearson coefficient of determination (R^2), the model skill was assessed quantitatively using model skill, root mean square error ($RMSE$), and percent bias ($\%BIAS$) (Fig. 3). Model skill is defined in the following manner:

$$SKILL = 1 - \frac{\sum_{k=1}^{L} \left(X_{\text{model}}^k - X_{\text{obs}}^k\right)^2}{\sum_{k=1}^{L} \left[\left|X_{\text{model}}^k - \overline{X}_{\text{obs}}\right| + \left|X_{\text{obs}}^k - \overline{X}_{\text{obs}}\right|\right]^2} \quad (3)$$

where X_{model}^k represents the modeled value and X_{obs}^k is the observed value respectively at time step k. The overbars are used to denote the time mean over the number of comparisons $k = 1, \ldots, L$. Skill values range between 1 and 0 with one representing perfect agreement and zero representing complete disagreement with the observed measurements. Mean skill scores for simulated stages are 0.95 with average

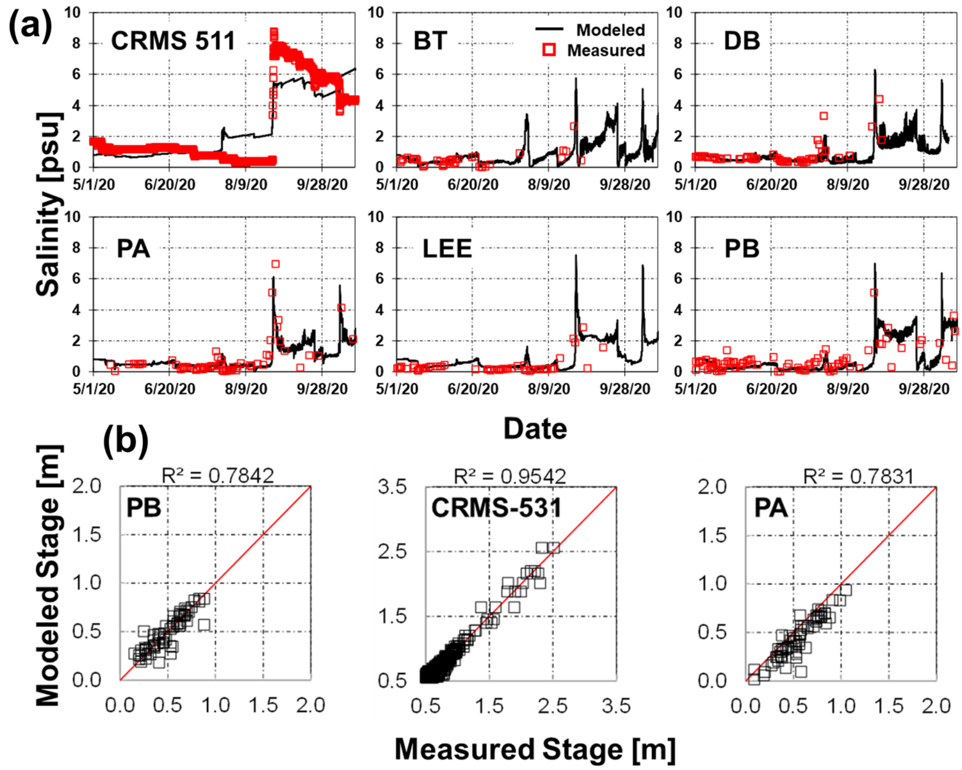

Fig. 3 (**a**) Model performance for instantaneous salinity at various locations. (**b**) Scatterplots for instantaneous stage (in meters NAVD 88 G99)

RMSE and %BIAS values of 0.11 m and − 7%, respectively, indicating that the model has high skill and performs acceptably well for predicting instantaneous stages (Table 1). The mean skill, *RMSE*, and *%BIAS* metrics for salinity are 0.76, 0.9 psu, and 11.6%. Overall, the results suggest that the model performs acceptably well in terms of simulating instantaneous stage and salinity for the purpose of scenario testing. Notably, the 5.5-month time period of analysis and salinity performance statistics are very comparable to other recent work (Vargas et al. 2017) focusing on the RLSR-induced salinity response.

Description of Alternative Scenarios

The calibrated local hydrodynamic model was applied to simulate the RSLR-induced salinity response under various alternative conditions. The model simulates depth-integrated salinity, water level, depth-integrated velocity, and volumetric flux in both coordinate directions at 62,427 locations each representing 63 m × 63 m land parcels. The salinity results are reported on an hourly basis while the hydrodynamic results are reported at a 4-h increment.

The scenario analysis began by defining the area of interest Ω_{AOI} on which comparisons would be made where Ω_{model} denotes the computational domain; hence, $\Omega_{AOI} \subset \Omega_{model}$. Furthermore, the partition $\Omega_{AOI} = \Omega_{OW} \cup \Omega_{FP}$ is imposed where OW and FP denote floodplain grid points classified based on elevation relative to the mean tide level. Further excluded from subsets of Ω_{AOI} were all points falling upland of the coastal zone boundary, points in the offshore bay region, and upland points located on the Avery Island salt dome. The OW/FP partition was kept the same over the

Table 1 Statistical measures of model performance. Stage comparisons were restricted to the three locations where a reliable vertical datum could be established. *N* is the number of instantaneous salinity comparison points

Location	Stage			Salinity			
	SKILL	*RMSE* [m]	*%BIAS*	*SKILL*	*RMSE* [psu]	*%BIAS*	*N*
CRMS-511	-	-	-	0.93	1.18	− 3%	4153
CRMS-531	0.99	0.06	3%	0.54	2.27	68%	3196
BT	-	-	-	0.69	0.38	9%	37
LEE	-	-	-	0.70	0.48	41%	59
PB	0.92	0.10	− 2%	0.74	0.77	− 12%	83
DB	-	-	-	0.85	0.45	− 11%	53
PA	0.95	0.16	− 21%	0.82	0.80	− 12%	66

scenarios to facilitate consistency in comparisons between future vs. base conditions.

The relative sea level rise effect was simulated by applying a uniform datum shift to the downstream tidal boundary conditions in discrete step increments. A 1-m range of increase in relative sea level was considered noting that accelerated rates of RSLR currently exist on the Louisiana coast (Tornqvist et al. 2020). Tornqvist et al. (2020) proposed an overall present day RSLR rate of 12 mm/year for Louisiana while Penland and Ramsey (1990) reported a RSLR rate of 14 mm/year for the Teche Basin (which includes the study area). Boon et al. (2018) suggest a weakly accelerating SLR rate is occurring at Grand Isle, LA, located to the east of the study area. Assuming a purely linear trend, the projected RSLR from 2021 to 2100 (79 years) is 0.948 and 1.11 m using the published values from Tornqvist et al. and Penland, respectively. The 1.0-m endpoint value analyzed in the forthcoming RSLR scenarios falls within this range. The 1.0-m value is also within the range for long-term (50–100 year) planning and performance horizon for coastal management activities — although, Fig. 2c suggests this value may be optimistic compared to a recent trend in Vermilion Bay (1998–2020).

For each RSLR increment being analyzed, an initial water level condition was applied (uniformly in space) having the same value as the initial boundary time point. Enforcing hydrodynamic compatibility in this way minimizes numerical instabilities (i.e., "shock") associated with "warm-up" as the numerical model attempts to reach a new equilibrium. Initial sensitivity tests comparing scenarios with and without a 2-month warm-up period further confirmed that the salinity comparative analysis was not sensitive to the warm-up period. After completing these preliminary checks, three distinct sets of numerical simulation trials (A, B, and C) were developed and are described next.

Trial set A examines sensitivity of RSLR-induced salinity change to deterioration of the floodplain vegetation/marsh platform (note: edge erosion is not considered). Three values of RSLR are considered: + 0.0 m, + 0.2 m, and + 0.4 m. The bathtub assumption ignores vertical accretion, and hence, the floodplain elevations do not change in response to RSLR. The bathtub assumption was imposed in trial set A. Deterioration was modeled by reducing the floodplain Manning's roughness values and increasing the dispersion coefficients. On a physical basis, marsh deterioration should correlate positively with a reduction in the floodplain net resistance and an increase in turbulent dispersivity. To illustrate the roughness effects, Shih and Rahi (1982) developed the following expression $n = D^{\frac{2}{3}} X^{0.5} (2g)^{0.5}$ relating the Manning's n to the depth D in meters, vegetation density X (1/meter) and gravitational acceleration g (m^2/s). From this expression, it can be inferred that reducing the n value by a factor of 2 corresponds to a fourfold reduction in vegetation density for the same flow depth. When combined with three values for composite floodplain resistance ($n_{\mathrm{FP}} = 0.07$, 0.057, and $0.04\mathrm{s/m}^{\frac{1}{3}}$) and three values of the minimum dispersion coefficient ($D_{\mathrm{FP}} = 0.05, 0.10, 0.20\mathrm{m}^2/\mathrm{s}$), this first set of sensitivity runs yields a total of $3 \times 3 \times 3 = 27$ combination scenarios denoted by A1-A27. The reduced values for Manning's n and increased values for D_{FP} were taken for convenience over a range given the highly uncertain nature of predicting future deteriorated marsh flow resistance and dispersion regimes. A 1-month period (July 2020) which featured a modest salinity spike was the basis of trial set A.

Trial set B expanded the deterioration analysis in set A by analyzing the full range of eleven RSLR values (+ 0.0, + 0.1, …, + 0.9, + 1.0 m) for (1) base/existing parameters ($n_{\mathrm{FP}} = 0.07, D_{\mathrm{FP}} = 0.05$), (2) reduced hydraulic roughness of the floodplain ($n_{\mathrm{FP}} = 0.034, D_{\mathrm{FP}} = 0.05$), (3) increased dispersion coefficients in the floodplains ($n_{\mathrm{FP}} = 0.07, D_{\mathrm{FP}} = 2.5$), and (4) increased offshore salinity boundary by a factor of 2 with base/existing parameters ($n_{\mathrm{FP}} = 0.07, D_{\mathrm{FP}} = 0.05$). The rationale for the doubled salinity boundary simulation was primarily to test the sensitivity of the RSLR-induced salinity response to future boundary uncertainty (e.g., due to droughts). This yields four trial groups for a total of $11 \times 4 = 44$ simulation scenarios where the RSLR = + 0.0 m for each group served as the basis of the comparison. Expanding the range of RSLR values and enhancing the deterioration effects allowed for an analysis of the fate of the RSLR-induced salinity curves over the long run. For simplicity, the bathtub assumption was also invoked in trial set B and the same 1-month period was used as the comparison basis. The robustness of the short-term response to boundary effects and choice of analysis period is also tested by analyzing an increased offshore boundary and an extended 3-month period.

The final trial set (C) examines the RSLR-induced salinity response when explicitly taking into account dynamic adjustments in vertical elevations of the marsh. This trial set took the base/existing parameters for floodplain resistance and dispersion ($n_{\mathrm{FP}} = 0.07, D_{\mathrm{FP}} = 0.05$) while varying the RSLR values by + 0.0, + 0.4, + 0.6, + 0.8, and + 1.0 m. In the spirit of the process model described in (Jankowski et al. 2017), a given floodplain location exhibits an accretion deficit when the vertical accretion rate is less than the rate of RSLR. Accretion surplus is defined analogously. In the absence of a detailed morphological model describing the temporal evolution of each elevation point in the domain, it was assumed that all sites currently exhibiting an accretion deficit would not keep pace with RSLR. The elevation of these vulnerable location points was held constant over all RSLR simulation scenarios in trial C. In similar fashion, sites currently exhibiting accretion surplus were presumed to all perfectly keep pace with RSLR. This analysis allows for a fixed (constant-in-time) partitioning of the floodplain symbol $\Omega_{\mathrm{FP}}^{X\%}$ where $X\%$ represents the percentage of areas under an accretion deficit. Noting the technical challenge of capturing the spatial configuration of $\Omega_{\mathrm{FP}}^{X\%}$ and the lack of accretion measurements spatially representative of the entire study domain (CRMS 511 and 531 are the only sites), an elevation cutoff criterion was employed based on published accretion deficit statistics for proximal regions in coastal Louisiana (Chenier Plain to the west, and Mississippi Delta to the east). The cutoff was defined by assuming that sites having lower elevations are more likely to exhibit accretion deficits compared to marsh sites having higher existing elevations.

Three scenarios were developed in trial C corresponding to the case where 100%, bottom 65%, and bottom 35% of the floodplain marshes are unable to keep pace with RSLR respectively (i.e., accretion deficit). The 65% and 35% values were chosen to approximate the percentage of CRMS sites experiencing accretion deficits in the western Chenier Plain and eastern Mississippi Delta — see (Jankowski et al. 2017). The cutoff elevations were established by examining the cumulative distribution of the existing digital topographic surface model elevation points comprising Ω_{FP}. The cutoff was then used to spatially delineate $\Omega_{\mathrm{FP}}^{65\%}$ and $\Omega_{\mathrm{FP}}^{35\%}$. For the marsh locations keeping pace, the elevations were adjusted stepwise by adding to them the incremental RSLR values in each simulation scenario. A 5-month period (May 1, 2020–October 1, 2020) was analyzed in addition to the 1-month July spike period as was the case in trials A and B.

Results

Trial Set A: Sensitivity to Marsh Deterioration Effects in the Short Term

The results show the relative sea level rise of + 0.2 and + 0.4 m would likely cause an increase in mean monthly salinities in open water areas (μ_S^{OW}) by 13% and 26% respectively compared to the base on average when considering the results of all scenarios (mean salinity increase). Salinities within the floodplain areas (μ_S^{FP}) increase by 57% and 97% respectively under the + 0.2 and + 0.4 RSLR scenarios where the percent change is based on the same set of floodplain grid cells. This result suggests that RSLR can be expected to impact salinities in adjacent floodplain habitats to a much greater degree than the open waters under the constant elevation case. For $n_{\mathrm{FP}} = 0.07$, 0.057, and 0.04, when averaging over the range of dispersion coefficients the open water areas experience increases in mean salinities of 25.6%, 25.9%, and 26.9% while the floodplains experience increases of 100.2%, 96.5%, and 94.4% compared to base when subjected to RSLR = + 0.4 m. Conversely, for $D_{\mathrm{FP}} = 0.05$, 0.1, and 0.2, when averaging over the range of roughness parameters, the open water areas experience increases in mean salinities of 26.3%, 26.0%, and 26.1% while the floodplains experience increases of 99.1%, 95.8%, and 96.3% compared to base when subjected to RSLR = + 0.4 m (Table 2).

Trial Set B: Sensitivity to Marsh Deterioration Effects in the Long Term

The mean salinity response was analyzed by comparing values against the mean water surface elevations relative to the current median elevation for the floodplain areas in the domain ($Z_{\mathrm{FP}}^{\mathrm{med}} = +0.87$ m). This same value for $Z_{\mathrm{FP}}^{\mathrm{med}}$ was taken as a constant vertical reference to facilitate consistent comparisons. The mean water surface relative to floodplain is given by $H_{\mathrm{R}} = \overline{H_{\mathrm{ow}}} - Z_{\mathrm{FP}}^{\mathrm{med}}$ where $\overline{H_{\mathrm{ow}}}$ is the mean open water surface elevation. The results suggest the existence of a nonlinear relationship between RSLR and salinity increase with the most drastic changes occurring before RSLR causes the mean water levels to exceed the current median floodplain elevations (Fig. 4). This nonlinear effect holds across all of the deterioration combinations investigated. The robustness of these effects was also tested by examining two additional scenarios which doubled the offshore boundary and extended the analysis period to 3 months. The extended period notably included a second salinity pulse associated with Hurricane Laura.

When $\overline{H_{\mathrm{ow}}} \geq Z_{\mathrm{FP}}^{\mathrm{med}}$, a saturating effect occurs whereby increasing relative sea levels no longer correspond with increasing salinities. As was the case in trial set A, the mean floodplain salinities surpass the mean salinities in the open water areas during the land loss progression. Increasing variability in the floodplain salinity response compared to the open water areas is also observed. This increase in variability is followed by a homogenization of floodplain salinities as the conversion their conversion to open water is completed (Fig. 4). Since this set of trials assumes the entire floodplain is at an accretion deficit, eventually all land is lost to RSLR and both salinity mean and variance in the floodplain converge to the open water values. Regression relationships were developed for the mean salinity response in floodplain areas (Table 3).

Trial Set C: Sensitivity to Dynamic Elevation Adjustments

Trial set B demonstrates a curvilinear relationship between $\mu_{\mathrm{S}}^{\mathrm{FP}}$ and $\mu_{\mathrm{S}}^{\mathrm{OW}}$ which shows a saturating behavior when $H_{\mathrm{R}} \geq 0$. The effect of accretion deficit/surplus on the curvilinear behavior of μ_{S} is now analyzed. First note that for floodplain areas under an accretion deficit, it is presumed that $Z_{\mathrm{FP}}(x, y, t) = Z_{\mathrm{FP}}(x, y)$ for all RSLR increments. For the other floodplain areas, their ability to uniformly keep pace is modeled by applying the rule $Z_{\mathrm{FP}}(x, y, t) = Z_{\mathrm{FP}}(x, y) + SLR(t)$. The model bathymetry for these areas is updated accordingly

Table 2 Summary of mean salinity sensitivity to floodplain parameter scenarios. The time period is the 31-day period of July 2020. The results illustrate the simulated effects of sea level rise under various combinations of floodplain parameters (mean hydraulic roughness n_{FP} and minimum dispersion coefficient D_{FP}) affecting the key transport processes of advection and dispersion respectively. The designation "b" represents the base case (zero RSLR) for each subgrouping of fixed parameters. *SE* is the standard error of the mean

Scenario ID	RSLR [m]	$n_{\mathrm{FP}}= 1/M_{\mathrm{FP}}$[s/m$^{1/3}$]	D_{FP} [m^2/s]	Mean salinity ± 1 *SE* [psu]	
				Open water	Floodplains
A1-b	+0.0	0.070	0.05	2.39 ± 0.08	1.62 ± 0.07
A1-1	+0.2	0.070	0.05	2.70 ± 0.08	2.67 ± 0.10
A1-2	+0.4	0.070	0.05	3.01 ± 0.08	3.36 ± 0.11
A2-b	+0.0	0.057	0.05	2.41 ± 0.08	1.71 ± 0.08
A2-1	+0.2	0.057	0.05	2.71 ± 0.08	2.68 ± 0.10
A2-2	+0.4	0.057	0.05	3.04 ± 0.08	3.36 ± 0.11
A3-b	+0.0	0.040	0.05	2.42 ± 0.08	1.75 ± 0.08
A3-1	+0.2	0.040	0.05	2.74 ± 0.08	2.72 ± 0.10
A3-2	+0.4	0.040	0.05	3.07 ± 0.08	3.39 ± 0.11
A4-b	+0.0	0.070	0.10	2.40 ± 0.08	1.71 ± 0.08
A4-1	+0.2	0.070	0.10	2.70 ± 0.08	2.67 ± 0.10
A4-2	+0.4	0.070	0.10	3.01 ± 0.08	3.35 ± 0.11
A5-b	+0.0	0.057	0.10	2.41 ± 0.08	1.71 ± 0.08
A5-1	+0.2	0.057	0.10	2.71 ± 0.08	2.68 ± 0.10
A5-2	+0.4	0.057	0.10	3.03 ± 0.08	3.36 ± 0.11
A6-b	+0.0	0.040	0.10	2.42 ± 0.08	1.74 ± 0.08
A6-1	+0.2	0.040	0.10	2.74 ± 0.08	2.72 ± 0.10
A6-2	+0.4	0.040	0.10	3.07 ± 0.08	3.39 ± 0.11
A7-b	+0.0	0.070	0.20	2.40 ± 0.08	1.70 ± 0.08
A7-1	+0.2	0.070	0.20	2.69 ± 0.08	2.67 ± 0.10
A7-2	+0.4	0.070	0.20	3.01 ± 0.08	3.35 ± 0.11
A8-b	+0.0	0.057	0.20	2.41 ± 0.08	1.70 ± 0.08
A8-1	+0.2	0.057	0.20	2.71 ± 0.08	2.67 ± 0.10
A8-2	+0.4	0.057	0.20	3.03 ± 0.08	3.35 ± 0.11
A9-b	+0.0	0.040	0.20	2.42 ± 0.08	1.74 ± 0.08
A9-1	+0.2	0.040	0.20	2.73 ± 0.08	2.71 ± 0.10
A9-2	+0.4	0.040	0.20	3.07 ± 0.08	3.39 ± 0.11

for each SLR increment. Here x and y denote spatial position, and t denotes a time in the future associated with a step increase in RSLR, e.g., $SLR(0) = 0.0\mathrm{m}$, $SLR(1) = +0.1\mathrm{m}$. For open waters, the bathymetry is static, and hence, $Z_{\mathrm{OW}}(x, y, t) = Z_{\mathrm{OW}}(x, y)$.

In addition to regional effects, local effects are studied in two sub-regions of interest which have the same spatial area measurement (Fig. 5(b.1)). These areas correspond to an oilfield marsh which is currently bisected by oilfield canals and spoil banks and a more natural marsh to the east of Avery Canal. The hydrodynamic model results are also used to approximate the volumetric flux occurring under each scenario. These fluxes are measured across transects located on the main tidal inlet (Avery Canal; FTS-2) and another larger transect which captures all flux being exchanged across the interior domain north of GIWW (FTS-1). The time-varying volumetric flow rates are denoted by $Q_{\mathrm{FTS}-n;i}$ (location and scenario denoted by n and i, respectively) and take the sign convention of positive flow occurring during rising tide (i.e., influx) and negative flow occurring during outflow periods. With this convention, the following definitions are made for cumulative inflow at a given time $t \in [0, T]$ where T is the end time of the simulation:

$$
\begin{aligned}
(V^+)_{n,c;i}\left(t^k\right) &= \int_0^{t^k} \max(\overline{Q_{\mathrm{FTS},n;i}(\tau)}^{\mathrm{daily}}, 0) d\tau \\
&\approx \sum_{s=0}^{k} \left(\frac{1}{6} \sum_{p=0}^{5} \max\left(Q_{\mathrm{FTS},n;i}(s+p), 0\right) \right) \Delta t
\end{aligned}
\tag{4}
$$

Here $(V^+)_{n,c;i}\left(t^k\right)$ represents cumulative inflow volume through transect n under RSLR scenario i at time t^k from the start of the simulation run. Also, k denotes the model output time step $k = 0, \ldots, L-6$, $t^k = k\Delta t$ where the model output time increment is $\Delta t = 4$ h, and $t^L = T$. The cumulative outflow is defined analogously and is denoted by the symbol $(V^-)_{n,c;i}\left(t^k\right)$. The overbar denotes the application of a (forward) daily moving average operator being applied to 4-h incremental outputs. Increases in cumulative inflow generally indicates a larger tidal prism and hence an enhanced potential for salinity intrusion. Since precipitation rates generally are comparable to ET in this area, it is expected that

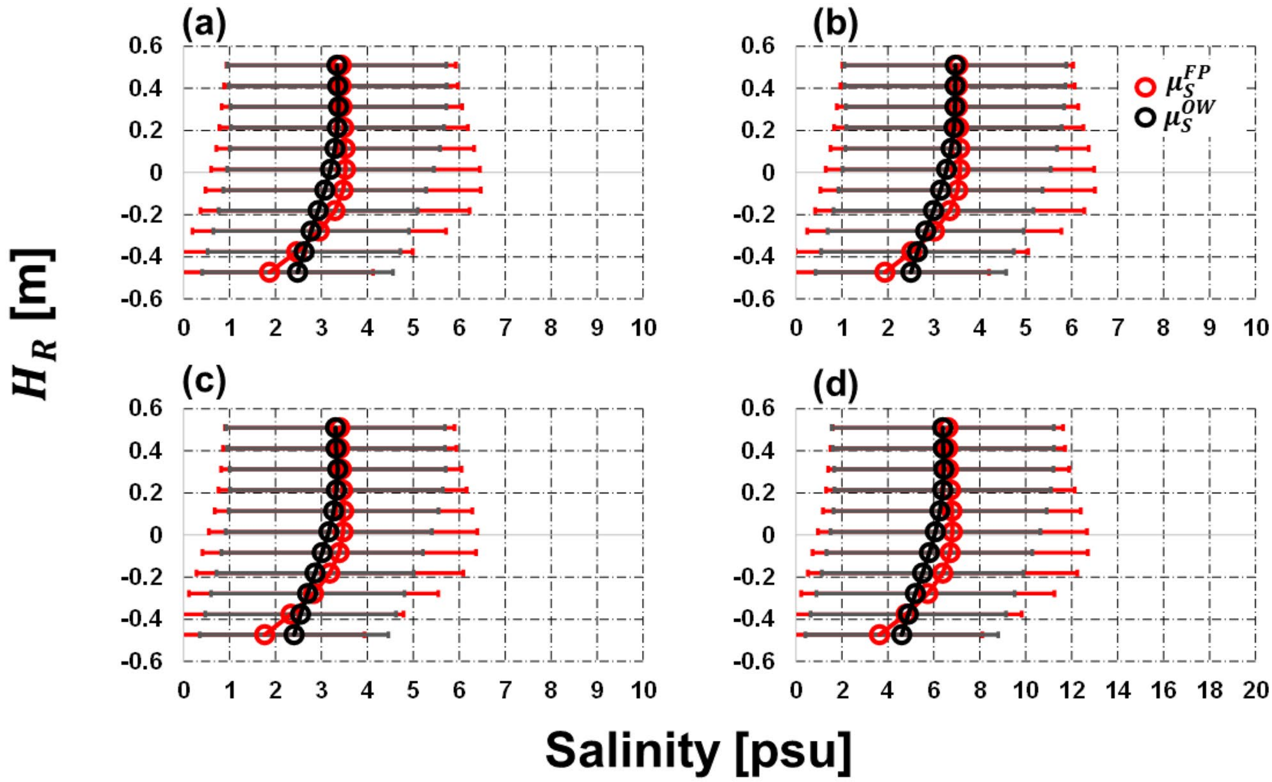

Fig. 4 Mean salinity (psu) in floodplain areas (red solid lines) and open water areas (black solid lines) for a range of sea level rise scenarios for the 1-month period (July 2020) which featured a 2-week salinity spike. The various cases represent (**a**) effects using base calibration parameters ($n_{\mathrm{FP}} = 0.07, D_{\mathrm{FP}} = 0.05$), (**b**) effects under reduced floodplain roughness ($n_{\mathrm{FP}} = 0.034, D_{\mathrm{FP}} = 0.05$), (**c**) effects under increased floodplain dispersion rates ($n_{\mathrm{FP}} = 0.07, D_{\mathrm{FP}} = 2.5$), (**d**) effects under doubling of the offshore salinity boundary condition with base parameters ($n_{\mathrm{FP}} = 0.07, D_{\mathrm{FP}} = 0.05$). Horizontal bars represent ± 1 SD which is an indicator of the mean salinity variability within the focus areas

$|V^-| \geq |V^+|$ due to temporary retention of incoming surface runoffs from upland areas. The difference in net cumulative inflow relative to the base/existing condition is

$$\Delta V_{n,c;i}^{\mathrm{inflow}}\left(t^k\right) = \left(V^+\right)_{n,c;i}\left(t^k\right) - \left(V^+\right)_{n,c;\mathrm{base}}\left(t^k\right) \quad (5)$$

and the change in net outflow ($\Delta V_{n,c;i}^{\mathrm{outflow}}\left(t^k\right)$) are defined by analogy. Ignoring any enhancement of sedimentation/shoaling effects, RSLR generally increases both $\Delta V_{n,c;i}^{\mathrm{inflow}}\left(t^k\right)$ and $\Delta V_{n,c;i}^{\mathrm{outflow}}\left(t^k\right)$ owing to a RLSR-induced increase in the cross-sectional flow area at tidal inlets.

Table 4 illustrates the preceding effects noting a general increase in tidal inflow and outflow volumes as a result of RSLR for the 1-month July spike scenario. Notably, the amplification of outflows is nearly an order of magnitude larger than the amplification of inflows both for the overall system inland (FTS-1) and the channel (FTS-2). By the comparison at FTS-1, reducing the accretion deficit from 100 to 65% reduces the overall inflow amplification from 54 to 48% under the RSLR = + 0.4 m scenario. Under this same scenario, reducing the accretion deficit further

Table 3 Nonlinear regression relationships for mean floodplain salinities $\mu_S^{FP}(H_R)$ (psu). Offshore time varying salinity boundary is denoted by S_o

n_{FP}	D_{FP}	S_o	Period	Relationship
0.07	0.05	Base	7/1–7/31	$\mu_S^{\mathrm{FP}}\left(H_R\right) = 5.1928H_R^3 - 3.941H_R^2 + 0.4894H_R + 3.5194(R^2 = 0.9988)$
0.034	0.05	Base	7/1–7/31	$\mu_S^{\mathrm{FP}}\left(H_R\right) = 5.2874H_R^3 - 3.8072H_R^2 + 0.4989H_R + 3.5664(R^2 = 0.9986)$
0.07	2.5	Base	7/1–7/31	$\mu_S^{\mathrm{FP}}\left(H_R\right) = 4.4896H_R^3 - 3.9631H_R^2 + 0.7355H_R + 3.4538(R^2 = 0.9987)$
0.07	0.05	2 × Base	7/1–7/31	$\mu_S^{\mathrm{FP}}\left(H_R\right) = 2(5.1125H_R^3 - 3.8003H_R^2 + 0.4299H_R + 3.4017)(R^2 = 0.9987)$
0.07	0.05	Base	7/1–9/30	$\mu_S^{\mathrm{FP}}\left(H_R\right) = 1.264H_R^3 - 2.1968H_R^2 + 1.2966H_R + 4.0959(R^2 = 0.9998)$

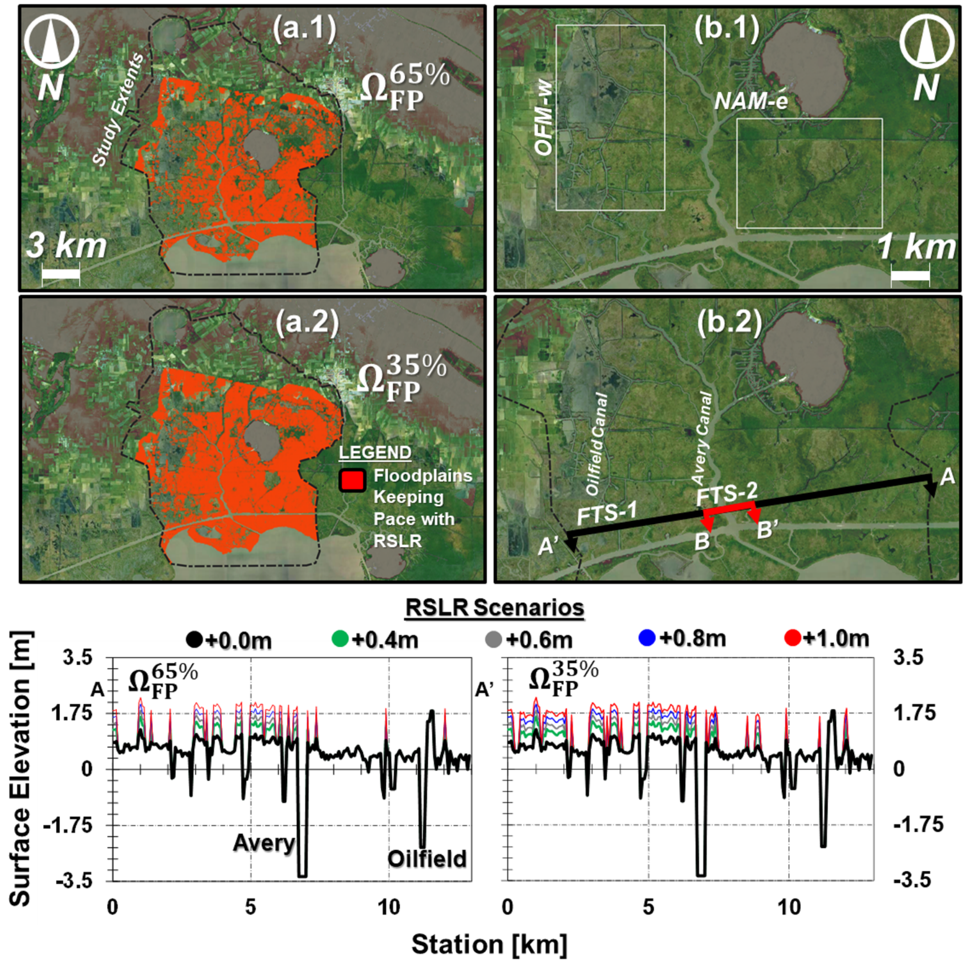

Fig. 5 (**a.1**, **a.2**) Red-colored areas depict the floodplain regions keeping pace under accretion deficits of 65% and 35%, respectively. (**b.1**) The two local sub-regions of interest — a relict oilfield marsh (OFM-w) and a natural marsh region (NAM-e). (**b.2**) Volumetric flux transects (FTS-1, FTS-2), and the bottom pane plots the model digital surface elevations along FTS-1 for the scenarios in trial C

from 65 to 35% causes an even greater reduction in the inflow amplification from 48 to 36%. For steadily increasing values of RSLR, the impact of reducing the accretion deficit in terms of hydraulic amplification becomes more pronounced. For RLSR = + 1.0 m, reducing the accretion deficit from 65 to 35% reduces the overall inflow amplification from 191 to 116%. Similar compound effects are observed for the RSLR-induced amplification of outflows. When restricting the analysis to the main channel inlet only (FTS-2), a similar pattern holds with lowering of the accretion deficit in the marsh corresponding to a reduction in the RSLR-induced amplification of outflow volumes in the channel.

The effects of the accretion deficit on RSLR-induced mean salinity follow directly from the hydraulic amplification effects. This is owing to the fact that larger inflow volumes generally correspond with larger salt transport into the estuary for the same inflow salinity. Figure 6 illustrates that larger accretion deficits in the marsh/floodplain exacerbate the nonlinear mean salinity increase to RSLR for both open water and floodplain habitats. Comparison of the analysis periods shows this effect is more pronounced

Table 4 Cumulative volume change compared to base scenario (RSLR = + 0.0 m) under varying marsh accretion deficits for the 1-month July 2020 salinity spike period

Transect	RSLR =	Increase in $\Delta V_{n,c;i}^{\text{inflow}}(T)$				Increase in $\Delta V_{n,c;i}^{\text{outflow}}(T)$				
		0.4 m	0.6 m	0.8 m	1.0 m	0.4 m	0.6 m	0.8 m	1.0 m	Ω_{FP}
FTS-1		54%	94%	140%	191%	332%	578%	856%	1168%	100%
		48%	73%	95%	116%	291%	444%	578%	705%	65%
		36%	50%	62%	76%	221%	308%	382%	467%	35%
FTS-2		31%	41%	45%	49%	205%	308%	363%	392%	100%
		32%	45%	53%	60%	195%	275%	319%	351%	65%
		27%	37%	43%	51%	159%	218%	265%	316%	35%

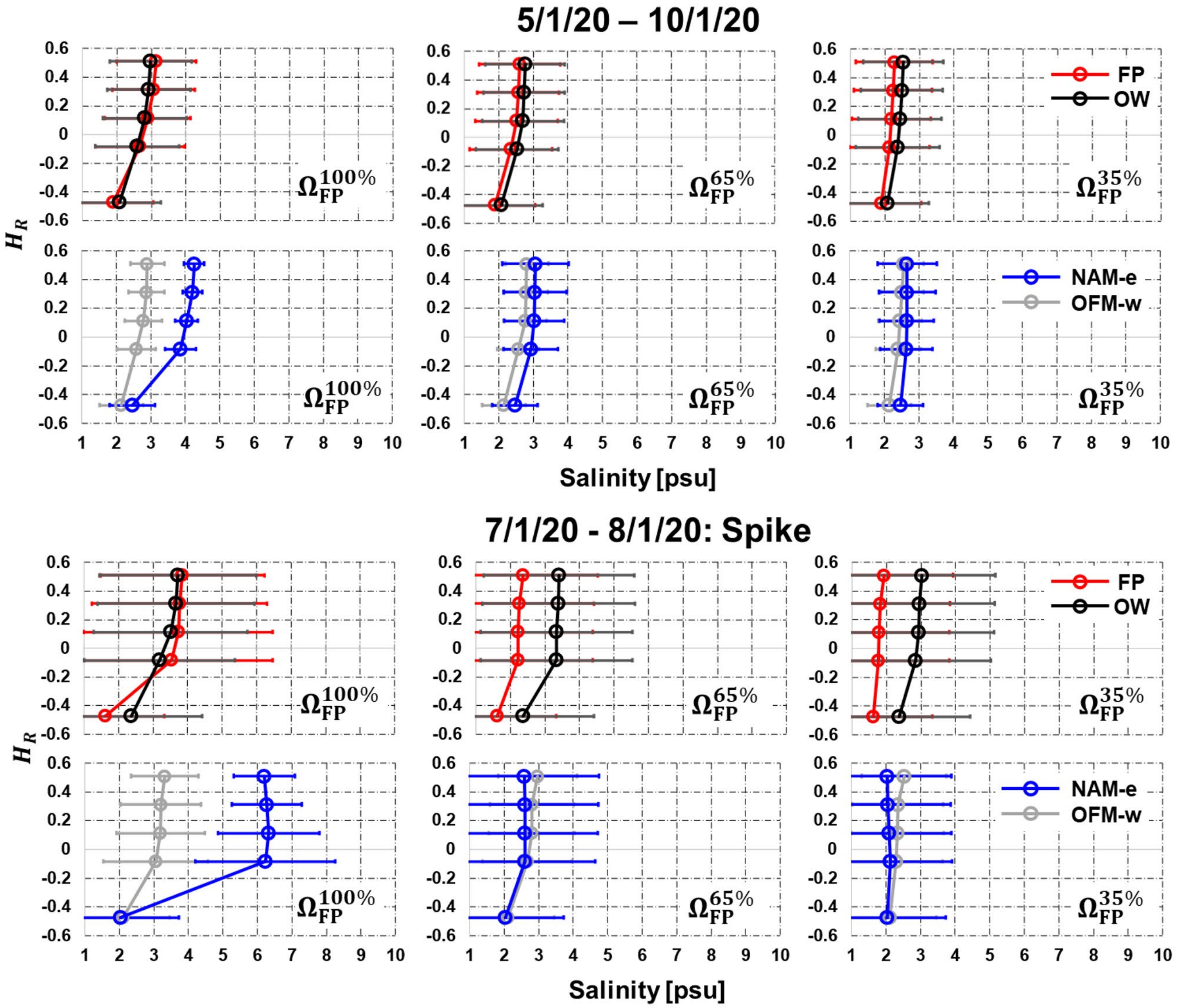

Fig. 6 Mean salinity response to RSLR (relative to the floodplain, H_R) under accretion deficits of 100%, 65%, and 35%. Note the period 5/1/20–10/1/20 period includes the relatively fresh months of May and June, while the July 1, 2020–August 1, 2020 period featured a modest salinity spike. FP and OW denote statistics over all floodplain and open water areas respectively within the coastal zone (excluding Avery Island). Horizontal bars represent standard deviations (SDs) which reflect the natural variability in salinities in the partitions. The results suggest greater sensitivity to RSLR-induced salinity response in the east natural marsh areas (NAM-e) compared to the marshes modified by oilfield activity (OFM-w) and similarly larger effects in existing floodplain areas vs. areas which have already converted to open water. Reducing the accretion deficit in the floodplains reduces the RSLR-induced salinity increase under both the longer (5-month) and shorter (spike) event time scales. The salinity variability is also preserved in the natural marsh areas by reducing the accretion deficit

during a salinity spike. Conversely, larger accretion surplus in the marsh tends to dampen the RSLR-induced nonlinearity — although this salinization dampening effect is less in the open water areas compared to directly inside the marsh regions. The local analysis provided in Fig. 6 further illustrates this point. There it is noted that the RSLR-induced nonlinear salinity increases in the oilfield marsh (generally consisting of more open water) are considerably less responsive to the overall accretion deficit of the region compared to more natural marsh sub-regions. However, the bottom pane of Fig. 6 demonstrates that preserving an accretion surplus in adjacent natural marshes can reduce the impact of RSLR-induced salinization in the oilfield marsh during spike periods by 25% at the + 1.0 m RSLR endpoint.

Discussion

Summary of Main Findings

A physically based approach is presented to model the RSLR-induced salinity response which accounts for nonlinear interactions between local drivers such as upland inflow, tidal range, marsh deterioration, and topographic variation both in space and time. The nonlinear RSLR-induced salinity response agrees with the initial findings reported by Yang et al. in their study on the Snohomish River estuary while providing a more detailed investigation of the nonlinearity (Yang et al. 2015). The results highlight the significance of the regional accretion deficit in the RSLR-induced salinity response in coastal floodplain areas. When the entire estuary region is under an accretion deficit, the bathtub assumption is invoked to model this case. Under this regime, the adjacent floodplain undergoes a nonlinear salinity response to RSLR scenarios based on mean water surface elevations relative to adjacent marsh. This finding is consistent with a simulation study whereby the authors demonstrate that sediment-poor regions are the most vulnerable to land loss under RSLR scenarios (White et al. 2019a, b). Although limited in its range of realistic applicability (Fagherazzi et al. 2019), a "bathtub" condition naturally arises in open water areas (such as tidal bays) or in floodplains artificially cut off from natural sedimentation processes. Examples of such sediment-deficient floodplain areas may include impoundments or agricultural fields in the coastal zone. Spoil banks (e.g., associated with canal dredging activity and municipal drainage enhancement) may also promote sediment starvation leading to large accretion deficits. Moreover, a recent study by Turner and Swenson (2020) reports that the abundance of spoil banks in coastal parishes of Louisiana has a combined length that is 80 times longer than the entire coast of Louisiana. Although the analysis shows the RSLR-induced salinization nonlinearity is somewhat affected by marsh deterioration rates, the balance between the mean elevations of land and water plays a role an order of magnitude larger than these factors together. By analyzing scenarios based on published accretion deficit prevalence in adjacent regions in coastal Louisiana (Jankowski et al. 2017), the findings underscore the importance of the accretion deficit in assessing the coastal wetland response (Reed and Cahoon 1993; Reed et al. 2020).

The analysis also suggests that hydraulic amplification (i.e., increasing inflows and outflow rates) from RSLR in open waters can be reduced somewhat by managing the accretion deficit in the surrounding floodplain. This finding is relevant for salinization management since the water balance (starting with the main channels) is a primary driver of salinity dynamics in coastal regions (and constituent transport more generally). Many coastal regions depend heavily on surface waters to support people activities, and increasing salinities is a global management concern (Minar et al. 2013). In a study on the Chesapeake Bay, the authors demonstrate upstream migration of critical salinity thresholds under RSLR scenarios (Rice et al. 2012). Increasing saltwater intrusion has also been cited as an increasing challenge in the Pearl River Delta in China (Gong and Shen 2011). Given the complexity of all the factors involved in shaping the RSLR-induced salinity response, the model-based approach taken in this study is complementary of previous efforts taken in this direction.

The analysis presented here did not consider effects which could exacerbate the RSLR-induced salinity response. Such factors include canal widening, accelerated subsidence, hurricane shears, or municipal interventions to mitigate upland riverine flooding (LWI 2020). The finding of amplification of the tidal exchange due to RSLR may accelerate shoreline erosion and canal widening compared to the present. As indicated in previous studies, coastal Louisiana is experiencing significant shoreline erosion (Scaife et al. 1983). Widening of canals has also been documented (Thatcher et al. 2010). Moreover, as indicated in the study following hurricanes Katrina and Rita, hurricane-induced "shears" of the marsh can cause abrupt conversion from marsh to open water (Barras 2007). Accelerated subsidence due to the extraction of petroleum fluids has also been noted in past studies which highlight localized affects and potential time-dependence of this dynamic (Mallman and Zoback 2007). Significant oilfield activities in the past and ongoing mining operations in the study region (e.g., associated with the salt domes) suggest the potential for accelerated subsidence to occur in this area. In light of the preceding factors the findings are likely conservative with respect to the RSLR-induced salinity changes and would likely underestimate the total cumulative effects.

Future Work

This study focused on the salinity response during a modest salinity spike which evolved during a one-month summer period prior to the hurricanes of 2020. It also examined a larger 5-month period (May 1, 2020–October 1, 2020) during the accretion deficit trials. The relative impacts of the RSLR-induced salinity response were demonstrated in the context of similar critical periods under various accretion/deterioration scenarios. Further research on the RSLR-induced mean salinity response during all seasons would help to better understand the effects of this dynamic throughout the year. The numerical model performance was sufficient for the current study but some improvements can be made. One challenge was establishing accurate stage measurements and datum consistency. Additional instantaneous stage readings having reliable datums would help in this regard — one example would be the use of GPS water level measurements (Cheng 2005). This is relevant for coastal Louisiana in light of current subsidence rates (Shinkle and Dokka 2004). A minimum floodplain dispersion factor of 0.05 m^2/s (for existing conditions) was applied in the absence of dye/tracer studies in the area. Prior studies reveal a wide range of variation in estuarine dispersion coefficients in general, and additional field measurements would help to reduce the uncertainty associated with this aspect of the modeling (West et al. 1990; Jabbari et al. 2004). The simulation scenarios were also limited to 1-month and 5-month summer periods and hence did not consider the effects of seasonality — particularly during fall and early spring.

Aside from a test of robustness with respect to the boundary condition in trial B, it was presumed that the offshore salinity boundary does not change as a result of RSLR. This assumption does not disagree with previous work on the Louisiana coast which detected statistically significant trends in estuarine salinity at many stations but no apparent underlying pattern in space (Wiseman et al. 1990). However, with uncertainties surrounding quality control of historical salinity records and consistency in record-keeping methods, it is unclear whether nearshore boundary salinities are increasing in coastal Louisiana (Wiseman et al. 1990). It is reasonable to expect that the spatial position of the riverine freshwater plumes will also adjust to future RSLR. Conversely, the river discharge associated with these plumes affects local RSLR rates (Piecuch et al. 2018). The trend of increasing river discharge on the Mississippi and Atchafalaya further complicates future predictions (Tao et al. 2014).

For the stepwise-based accretion deficit partitioning, it was assumed the accretion deficits are most likely concentrated in sites having a lower existing average marsh elevation. A more flexible approach would allow for greater spatial heterogeneity owing to physical factors such as proximity to the sediment supply and marsh vegetation types. Note also that larger inflow volumes associated with RSLR-induced hydraulic amplification can result in net sediment import which may affect the accretion deficit in the adjacent floodplains. Differential accretion or subsidence rates occurring at different spatial locations in the domain were also not analyzed. Given the time-varying nature of these local factors, a more physically accurate accretion deficit partitioning should also be time-varying as well.

Another challenge associated with RSLR/salinity response studies, most notably for predominantly brackish/intermediate estuaries, are the relatively low existing salinities. This makes numerical model calibration and validation in these regions more difficult because there are usually fewer salinity measurements showing enough variability to support tuning of the parameters. Also, model performance in these settings would be more sensitive to errors given the lack of variance in the existing salinity signals, e.g., it can be easily shown that some commonly used statistical performance metrics such as Nash–Sutcliffe Efficiency (NSE) decrease as the mean squared deviation in the measurements decreases (Gupta and Kling 2011). Moreover, in this study, the upland limits of the local hydrodynamic model were fixed based on the existing coastal zone boundary delineation but future sea level rise would naturally lead to inland adjustments of these zones (Fagherazzi et al. 2019). The nesting strategy employed to couple the regional hydrologic and local hydrodynamic models allows some flexibility in dealing with the uncertainty of the future location of the upland boundary.

Conclusions

This study presents a physically based two-dimensional modeling approach to study the critical coastal management problem of RSLR-induced salinity changes in the coastal zone. The study focused on brackish floodplain regions which have been less studied compared to RSLR-induced salinity in open water areas or salt marsh systems. The calibrated model is used to investigate nonlinear process interactions (e.g., marsh flow resistance and dispersion factors) and the role played by the accretion deficit on the RSLR-induced salinity response in coastal floodplains. The results highlight that the accretion deficit will likely play a major role in shaping the overall salinity response to RSLR. The fraction of the floodplain which is able to keep pace with RSLR has an effect an order of magnitude larger than transport parameters associated with marsh deterioration. Sites exhibiting sustained accretion surpluses over the long term are able to keep pace and would likely contribute to greater overall resilience to future RSLR-induced salinity changes. Under rising sea levels, these areas would also most likely preserve their natural salinity variability in comparison to other more vulnerable marshes — a finding which is significant for biodiversity preservation (Galvan et al. 2016). The results further demonstrate the effects of the accretion deficit on the regional hydraulics with reductions in overall RSLR-induced hydraulic amplification associated with a higher accretion surplus. In this regard, coastal management efforts which target the establishment or maintenance of an accretion surplus in the floodplain should be a priority towards managing the RLSR-induced salinity response. The findings also highlight the value of regional stakeholder investment in comprehensive marsh elevation monitoring networks in efforts to manage and mitigate future RSLR-induced challenges.

Acknowledgements The author would like to thank three anonymous referees for their insightful suggestions which improved the manuscript. The author would also like to thank the United States Geological Survey (USGS), the Louisiana State University (LSU) Atlas-LiDAR Project, the LSU AgCenter Iberia Research Center, the National Oceanic and Atmospheric Administration, and Louisiana's Coastwide Reference Monitoring System for providing the technical data needed perform the study.

Funding This research was supported in part by the Louisiana Board of Regents Support Fund LEQSF (2020–23)-RD-A-25, and the National Academies of Science, Engineering, and Medicine Gulf Research Fellowship Program.

Data Availability The data that support the findings of this study are available from the corresponding author upon reasonable request.

Declarations

Conflict of Interest The author declares no competing interests.

References

Autin, W. 2002. Landscape evolution of the Five Islands of south Louisiana: Scientific policy and salt dome utilization and management. *Geomorphology* 47: 227–244.

Barras, J. 2007. Land area changes in coastal Louisiana after Hurricanes Katrina and Rita - science and the storms-the USGS response to the hurricanes of 2005 (Circular 1306). Reston, VA: USGS.

Bhuiyan, M., and D. Dutta. 2012. Assessing impacts of sea level rise on river salinity in the Gorai river network. *Estuarine, Coastal and Shelf Science*, 219–227.

Boon, J., M. MItchell, J. Loftis, and D. Malmquist. 2018. Anthropocene sea level change: a history of recent trends observed in the U.S. East, Gulf, and West Coast regions. Gloucester Point, VA: Virginia Institute of Marine Science, William & Mary.

Cahoon, D. 2015. Estimating relative sea-level rise and submergence potential at a coastal wetland. *Estuaries and Coasts* 38: 1077–1084.

Cheng, K. 2005. *Analysis of water level measurements using GPS*. Columbus, OH USA: The Ohio State University.

Church, J., and N. White. 2011. Sea-level rise from the late 19th to the early 21st century. *Surveys in Geophysics* 32: 585–602.

Coastal Protection and Restoration Authority (CPRA) of Louisiana. 2021. Coastwide Reference Monitoring System - Wetlands Monitoring Data. Retrieved from Coastal Information Management System (CIMS) database. https://cims.coastal.louisiana.gov. Accessed 14 December 2020.

Cunningham, R., D. Gisclair, and J. Craig. 2004. The Louisiana Statewide Lidar Project. Baton Rouge, LA: Louisiana State University.

DHI. 2017. MIKE 21 Flow Model & MIKE 21 Flood Screening Tool. Horsholm, Denmark: Danish Hydraulic Institute.

Fagherazzi, S., S.B. Anisfield, E. Long, R. Feagin, A. Fernandes, W. Kearney, and K. Williams. 2019. Sea level rise and the dynamics of the marsh-upland boundary. *Frontiers in Envieronmental Science*. https://doi.org/10.3389/fenvs.2019.00025.

Fontenot, R. 2004. An evaluation of reference evapotranspiration models in Louisiana - Masters Thesis. Baton Rouge, LA: Louisiana State University Digital Commons.

Galvan, C., A. Puente, S. Castanedo, and J. Juanes. 2016. Average vs. extreme salinity conditions: Do they equally affect the distribution of macroinvertebrates in estuarine environments? *Limnology and Oceanography* 61: 984–1000.

Gong, G., and J. Shen. 2011. The response of salt intrusion to changes in river discharge and tidal mixing during the dry season in the Modaomen Estuary. *China. Continental Shelf Research* 31 (7–8): 769–788.

Gupta, H., and H. Kling. 2011. On typical range, sensitivity, and normalization of mean squared error and Nash-Sutcliffe efficiency type metrics. *Water Resources Research* 47: 1–3.

Hernandez, M., W.M Hill, D. Clark, B. Flusche, M. Fuselier, D. Griffin III, . . . D. Williams. 1976. *Environmental study of Lake Peigneur, a tidal lake*. Lafayette, LA: National Science Foundation.

Ho, D., V. Engel, E. Variaon, P. Schmieder, and M. Condon. 2009. Tracer studies of sheet flow in the Florida Everglades. *Geophysical Research Letters* 36: 1–6.

Hong, B., and J. Shen. 2012. Responses of estuarine salinity and transport processes to potential future sea-level rise in the Chesapeake Bay. *Estuarine, Coastal and Shelf Science* 104–105: 33–45.

Huang, W., S. Hagen, P. Bacopoulos, and D. Wang. 2015. Hydrodynamic modeling and analysis of sea-level rise impacts on salinity for oyster growth in Apalachicola Bay, Florida. *Estuarine, Coastal and Shelf Science* 156: 7–18.

Jabbari, E., R. Bozorgi, and A. Etemad-Shahidi. 2004. Longitudinal dispersion coefficients in estuaries. *SI 39* (pp. 537–541). Itajai, Brazil: Journal of Coastal Research.

Jankowski, K., T. Tornqvist, and A. Fernandes. 2017. Vulnerability of Louisiana's coastal wetlands to present-day rates of relative sea-level rise. *Nature Communications* 8: 14792. https://doi.org/10.1038/ncomms14792.

Krvavica, N., and I. Ruzic. 2020. Assessment of sea-level rise impacts on salt-wedge intrusion in idealized and Neretva River Estuary. *Estuarine, Coastal and Shelf Science* 106638.

Krvavica, N., B. Mofardin, I. Ruzic, and N. Ozanic. 2012. Measurement and analysis of salinization of the Rjecina estuary. *Gradevinar* 64: 923–933.

Liu, W., and H.-M. Liu. 2014. Assessing the impacts of sea level rise on salinity intrusion and transport time scales in a tidal estuary. *Taiwan. Water* 6: 324–344.

LWI. (2020). *State to begin funding flood mitigation priorities with $1.2 billion line of credit*. Retrieved from Louisiana Watershed Initiative Press Release. https://www.watershed.la.gov/news/press-releases/state-to-begin-funding-flood-mitigation-priorities-with-1-2-billion-line-of-credit.

Mallman, E., and M. Zoback. 2007. Subsidence in the Louisiana Coastal Zone due to hydrocarbon production. *Journal of Coastal Research Special Issue* 50: 443–448.

Miller, R., and E. Meselhe. 2007. Louisiana Chenier plain regional hydrodynamic and salinity numerical model. *10th Annual International Conference on Estuarine and Coastal Modeling*. Providence, RI: American Society of Civil Engineers. https://doi.org/10.1061/40990(324)25.

Minar, M., M. Hossain, and M. Shamsuddin. 2013. Climate change and coastal zone of Bangladesh: Vulnerability, resilience and adaptability. *Middle-East Journal of Scientific Research* 13 (1): 114–120.

Morris, J., P. Sundareshwar, C. Nietch, B. Kjerfve, and D. Cahoon. 2002. Responses of coastal wetlands to rising sea level. *Ecology* 83 (10): 2869–2877.

Mossa, J. 2016. The changing geomorphology of the Atchafalaya River, Louisiana: a historical perspective. *Geomorphology*, 112–127.

NOAA. 2021. *NOAA Chart* 11345. Retrieved from NOAA Office of Coast Survey. https://www.charts.noaa.gov/PDFs/11345.pdf.

Pathikonda, S., A. Ackleh, K. Hasenstein, and S. Mopper. 2008. Invasion, disturbance, and competition: Modeling the fate of coastal populations. *Conservation Biology* 23 (1): 164–173.

Penland, S., and K. Ramsey. 1990. Relative sea-level rise in Louisiana and the Gulf of Mexico: 1908–1988. *Journal of Coastal Research*, 323–342.

Piecuch, C., K. Bittermann, A. Kemp, R. Ponte, C. Little, S. Engelhart, and S. Lentz. 2018. River-discharge effects on United States Atlantic and gulf coast sea-level changes. *Proceedings of the National Academy of Sciences of the United States of America* 115 (30): 7729–7734.

Price, R. 2020. *Louisiana Agriclimatic Information System*. Retrieved from LSU Agcenter. https://weather.lsuagcenter.com/.

Reed, D., and D. Cahoon. 1993. Marsh submergence vs. marsh accretion: interpreting accretion deficit data in coastal Louisiana. *8th Symposium on Coastal and Ocean Management* (pp. 243–257). New Orleans: Coastal Zone 93.

Reed, D., Y. Wang, E. Meselhe, and E. White. 2020. Modeling wetland transitions and loss in coastal Louisiana under scenarios of future relative sea-level rise. *Geomorphology* 352: 106991.

Rice, K., B. Hong, and J. Shen. 2012. Assessment of salinity intrusion in the James and Chickahominy Rivers as a result of simulated sea-level rise in Chesapeake Bay, East Coast, USA. *Journal of Environmental Management* 111: 61–69.

Saad, H., E. Habib, and R. Miller. 2020. Effect of model setup complexity on flood modeling in low-gradient basins. *Journal of American Water Resources Association*. https://doi.org/10.1111/1752-1688.12884.

Scaife, W., R. Turner, and R. Costanza. 1983. Coastal Louisiana recent land loss and canal impacts. *Environmental Management* 7 (5): 433–442.

Shih, S., and G. Rahi. 1982. Seasonal variations of Manning's roughness coefficient in a subtropical marsh. *Transactions of the American Society of Agricultural Engineers* 25 (1): 116–119.

Shinkle, K., and R. Dokka. 2004. *Rates of vertical displacement at benchmarks in the lower Mississippi Valley and the Northern Gulf Coast*. Washington, DC: National Oceanic and Atmospheric Administration.

Spalding, E., and M. Hester. 2007. Interactive effects of hydrology and salinity on oligohaline plant species productivity: Implications of relative sea-level rise. *Estuaries and Coasts* 30 (2): 214–225.

Sullivan, J., R. Torres, A. Garrett, J. Blanton, C. Alexander, M. Robinson, … D. Hayes. 2015. Complexity in salt marsh circulation for a semienclosed basin. *Journal of Geophysical Research Earth Surface* 120: 1973–1989.

Sunde, J., C. Tamario, P. Tibblin, P. Larsson, and A. Forsman. 2018. Variation in salinity tolerance between and within anadromous subpopulations of pike (Esox lucius). *Nature Scientific Reports* 8: 22. https://doi.org/10.1038/s41598-017-18413-8.

Tao, B., H. Tian, W. Ren, J. Yang, Q. Yang, R. He, … S. Lohrenz. 2014. Increasing Mississippi river discharge throughout the 21st century influenced by changes in climate, land use, and atmospheric CO2. *Geophysical Research Letters* 41: 4978–4986.

Thatcher, C., S. Hartley, and S. Wilson. 2010. Bank erosion of navigation canals in the western and central Gulf of Mexico: U.S. Geological Survey Open File Report 2010–1017 and OCS Study BOEMRE 2010–039. Lafayette, LA: USGS National Wetlands Research Center.

Tornqvist, T.E., K.L. Jankowski, Y.X. Li, and J.L. Gonzalez. 2020. Tipping points of Mississippi Delta marshes due to accelerated sea-level rise. *Science Advances* 6 (21). https://doi.org/10.1126/sciadv.aaz5512.

Turner, R., and E. Swenson. 2020. The life and death consequences of canals and spoil banks in salt marshes. *Wetlands* 40: 1957–1965.

USDA. 2021. *NRCS soil map*. Retrieved from Web Soil Survey. https://websoilsurvey.sc.egov.usda.gov/App/WebSoilSurvey.aspx.

Vargas, C., N. Vaz, and J. Dias. 2017. An evaluation of climate change effects in estuarine salinity patterns: Application to Ria de Aveiro shallow water system. *Estuarine, Coastal and Shelf Science* 189: 33–45.

Visser, J., C. Sasser, R. Linscombe, and R. Chabreck. 2000. Marsh vegetation types of the Chenier Plain, Louisiana, USA. *Estuaries* 23 (3): 318–327.

West, J., R. Uncles, J. Stephens, and K. Shiono. 1990. Longitudinal dispersion processes in the Upper Tamar Estuary. *Estuaries* 13 (2): 118–124.

White, E., E.R. Meselhe, A. Renfro, N. Snider, and Y. Wang. 2019a. Mitigating the effects of sea-level rise on estuaries of the Mississippi Delta plain using river diversions. *Water* 11. https://doi.org/10.3390/w11102028.

White, E., D. Reed, and E. Meselhe. 2019b. Modeled sediment availability, deposition, and decadal land change in Coastal Louisiana marshes under future relative sea level rise scenarios. *Wetlands* 39: 1233–1248.

Wiseman, W., Jr., E. Swenson, and J. Power. 1990. Salinity trends in Louisiana estuaries. *Estuaries* 13 (3): 265–271.

Yang, Z., T. Wang, N. Voisin, and A. Copping. 2015. Estuarine response to river flow and sea-level rise under future climate change and human development. *Estuarine, Coastal and Shelf Science* 19–30.